Nanostructured 2D cellular materials in silicon by sidewall transfer lithography NEMS

2017 J. Micromech. Microeng. 27 075003

(http://iopscience.iop.org/0960-1317/27/7/075003)

IOP Publishing Journal of Micromechanics and Microengineering
J. Micromech. Microeng. **27** (2017) 075003 (15pp) https://doi.org/10.1088/1361-6439/aa7167

Nanostructured 2D cellular materials in silicon by sidewall transfer lithography NEMS

Richard R A Syms, Dixi Liu and Munir M Ahmad

EEE Department, Imperial College London, Exhibition Road, London SW7 2AZ, United Kingdom

E-mail: r.syms@imperial.ac.uk

Received 6 February 2017, revised 12 April 2017
Accepted for publication 5 May 2017
Published 2 June 2017

Abstract

Sidewall transfer lithography (STL) is demonstrated as a method for parallel fabrication of 2D nanostructured cellular solids in single-crystal silicon. The linear mechanical properties of four lattices (perfect and defected diamond; singly and doubly periodic honeycomb) with low effective Young's moduli and effective Poisson's ratio ranging from positive to negative are modelled using analytic theory and the matrix stiffness method with an emphasis on boundary effects. The lattices are fabricated with a minimum feature size of 100 nm and an aspect ratio of 40:1 using single- and double-level STL and deep reactive ion etching of bonded silicon-on-insulator. Nanoelectromechanical systems (NEMS) containing cellular materials are used to demonstrate stretching, bending and brittle fracture. Predicted edge effects are observed, theoretical values of Poisson's ratio are verified and failure patterns are described.

Keywords: cellular solids, nanoelectromechanical systems, sidewall transfer lithography

(Some figures may appear in colour only in the online journal)

1. Introduction

Microfabricated silicon sensors are incorporated in many advanced products [1, 2]. Success can be ascribed to a combination of material properties [3] and compatible processes [4]. However, because the use of other materials introduces process complications, performance is generally determined by the properties of Si itself. Here we consider whether structuring may modify its effective properties. This approach has had strong appeal in electromagnetics, where it is known as 'metamaterials' [5], especially to obtain novel behaviour [6].

In mechanical engineering, structured media are known as cellular solids [7, 8]. The arrangement can be a two-dimensional (2D) [9] or 3D lattice [10], aperiodic lattice [11] or foam [12]. The effective elastic moduli and Poisson's ratio of many cells have been derived [13–17], together with their failure modes [18–21] and dynamic properties [22, 23]. There is interest in unusual properties, such negative [24–26] or zero [27] values of Poisson's ratio. Strains can be larger than in conventional media; however, responses are mainly anisotropic and non-linear. Other controllable properties include thermal conductivity [28] and expansion coefficient [29]. 2D periodic structures are generally fabricated by extrusion [30], while aperiodic materials are often foams [31]. Applications include heat exchangers, aerospace components, packaging and stents, and there are analogies with biological materials such as wood and trabecular bone [32].

Because their properties can be controlled by layout, cellular solids should offer advantages in nanoelectromechanical systems (NEMS). Applications include piezo-composites [33, 34], acoustic materials [35, 36] and mechanisms [37–39]. However, formation of structured microscale parts requires nanofabrication. Existing methods have been reviewed in [40]. For 2D materials, these include soft lithography and moulding [41] and deep reactive ion etching (DRIE) [42]. For 3D materials, x-ray lithography [43], direct laser writing [44], stereo-lithography [45], 3D printing [46] and folding [47] have been proposed. However, only 2D processes are currently compatible with integration. Although this limits the range of materials, many devices may still benefit. Examples range from seismometers (which require low suspension stiffness in the sensitive direction) and thermal sensors (which require low thermal conduction). Even so, there are problems preventing exploitation. The most flexible processes use photopolymers, and it is difficult to reduce wall thickness below around 0.5 μm without expensive serial patterning.

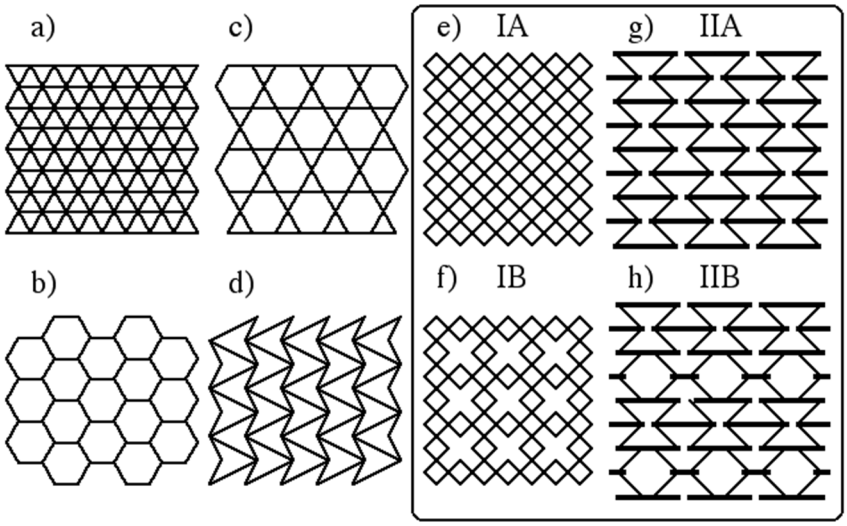

Figure 1. (a) Triangular, (b) hexagonal, (c) trihexagonal, (d) auxetic quadrilateral, (e) diamond, (f) defected diamond, (g) re-entrant honeycomb, (h) zero Poisson's ratio lattices.

In this paper we demonstrate 2D nanostructured materials that can be integrated directly into silicon NEMS using a parallel fabrication process, sidewall transfer lithography (STL). STL was developed to overcome resolution limits in microelectronics [48, 49], but has since been modified to fabricate optics [50, 51], field emission devices [52], nanowires [53, 54], nanoimprint templates [55, 56], photomasks [57] and nanochannels [58]. We ourselves have used it to fabricate single crystal NEMS [59, 60], by DRIE of bonded silicon-on-insulator (BSOI) [61, 62]. Here we use demonstrate cellular materials. In section 2, we consider the linear mechanical properties of four lattices with different effective parameters, using stiffness matrix models and focusing on the validity of the effective medium approximation in geometries with boundaries. In section 3, we describe the fabrication of suspended silicon devices containing cellular material using STL patterning of BSOI. In section 4, we present experimental results, and show that many of the theoretical predictions can be observed directly. Conclusions are drawn in section 5.

2. Cellular materials and devices

In this section, we review the characteristics of 2D cellular solids, using simple models to demonstrate the behaviour of lattices that may be formed using STL NEMS.

2.1. Cellular materials

Figure 1 shows eight well-known cellular materials, with triangular (a), hexagonal (b), trihexagonal (c), diamond (e), defected diamond (f), negative Poisson's ratio (d), (g) and zero Poisson's ratio (h) (NPR and ZPR) lattices [7–9, 13–16, 25–27]. Some (hexagonal, defected diamond) are flexible, while others (triangular) are stiff. Their linear, non-linear and failure properties have all been investigated. Briefly, a linear response is obtained when deflections lie in the linear regime. However, the response may become non-linear at moderate displacements, due to geometric effects or buckling. Irreversible non-linearity may emerge as plastic hinges develop or brittle fracture occurs [7], and cracks may propagate following a cellular analogue of the Griffith mechanism [20, 21]. Here we focus on the highlighted lattices, whose significance is that all may be fabricated using STL. The diamond (e) and defected diamond (f) lattices use flexible members of constant width; we term these IA and IB. The NPR (g) and ZPR (h) lattices use flexible diagonal and stiff horizontal members; we term these IIA and IIB.

2.2. Modelling

Previous analysis has mainly been for macroscopic applications. Similarly, apart from a few exceptions (e.g. [37, 38]), cellular materials have not formed part of complete devices. Here we give an overview relevant to NEMS, when behaviour is predominantly linear but cell numbers are relatively small and edge effects significant. Although finite element methods are often used to model cellular materials, their complexity and aspect ratio can cause difficulties. We therefore base the discussion on Euler bending theory (see e.g. [63]) and the stiffness matrix method [64, 65]. We restrict the analysis to 2D, assume deflections are linear and ignore shear.

For a single horizontal member of length L, the relation between the loads F_{xi} and F_{yi} in the x- and y-directions and moments M_{zi} about the z-axis at either end can then be related to the deflections u_{xi}, u_{yi} and θ_{zi} using the matrix elements in figure 2. Here E is Young's modulus, $A = wd$ is the cross-sectional area and $I = dw^3/12$ is the second moment of area for a member of depth d and width w. These elements cannot model axial shortening in bending, which introduces strain-dependence [39]. For an inclined member, rotation matrices are used to project forces into local co-ordinates and return deflections to global co-ordinates. Loads and deflections are propagated between members using compatibility conditions and the resulting equations solved subject to loads and

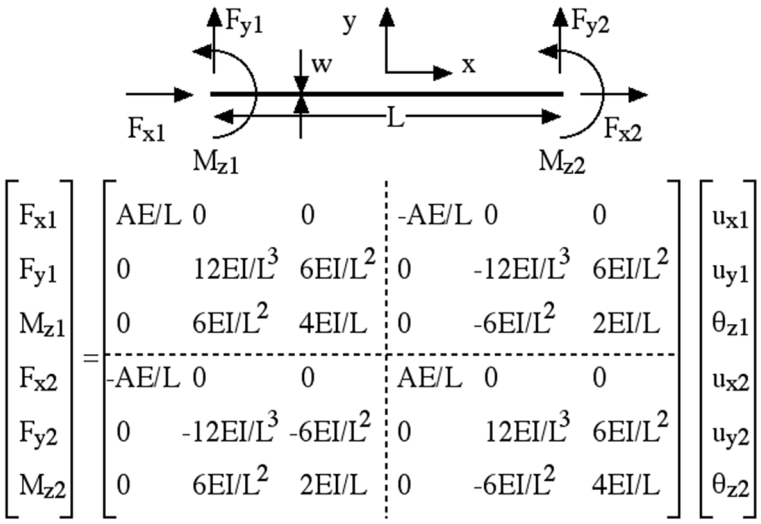

Figure 2. Stiffness matrix elements for a single horizontal structural member.

Table 1. Comparison of numerical and analytic values for E_0^* and v_0^* for a diamond lattice.

L (μm)	F_x (N)	ε_{xx}	σ_{xx} (N m^{-2})	E_0^*/E_{45} (numerical)	E_0^*/E_{45} (analytic)	v_0^* (numerical)	v_0^* (analytic)
1	1×10^{-5}	0.0069	1.768×10^{6}	2.000×10^{-3}	2×10^{-3}	0.9802	1.0000
10	1×10^{-7}	0.0068	1.768×10^{3}	1.998×10^{-6}	2×10^{-6}	0.9998	1.0000
100	1×10^{-9}	0.0068	1.768×10^{0}	2.000×10^{-9}	2×10^{-9}	1.0000	1.0000

constraints. We have developed MATLAB software to lay out lattices, apply loads and boundary conditions, solve the matrix problem and plot deflections in a few seconds.

2.3. Material properties

Crystalline silicon is mechanically anisotropic [3, 66]. We assume that lattices are formed in [1 0 0] wafers, with flexure in plane. For members lying in the x-direction, stress is predominantly in the [1 1 0] direction and we assume a Young's modulus $E_0 = 169 \times 10^9$ N m^{-2}; for members at 45° to the x- and y-axes, we assume $E_{45} = 130 \times 10^9$ N m^{-2} [67]. Although the members are narrow, we ignore the size effects in ultra-thin beams [68], so the mechanics are scale-independent. Silicon is also brittle. A commonly quoted figure for failure strength is 7×10^9 N m^{-2} [3], leading to a failure strain of ≈5%. However, much lower (0.5%–1.0%) values have been measured [69], depending on direction, size and surface condition [70].

2.4. Effective medium properties

For large lattices, the dependence of extension on load can be recast as a stress–strain relation with an effective value of Young's modulus. Accompanying this will be a transverse contraction, leading to an effective value of Poisson's ratio. Other properties, such as acoustic velocity and the resonant frequency of vibrating structures, can be determined from the appropriate value of effective elastic coefficient and the effective density. The aim of effective medium theory is to design on the basis of these values. Here we use matrix calculations to highlight its validity (or lack thereof). We focus initially on the IA diamond lattice, which is weak against normal forces but resists shear. In the results that follow, unloaded and loaded structures are outlined in grey and black.

Figure 3(a) shows the distortion of a single unit cell of side $L = 10$ μm, member width $w = 100$ nm and depth $d = 4$ μm due to horizontal tensile forces $F = 10^{-6}$ N at either end. Clearly, the cell has elongated in the x-direction and contracted in the y-direction. Expressing the load as a stress σ_{xx} and the elongation as a strain ε_{xx} allows calculation of an equivalent Young's modulus $E_0^* = \sigma_{xx}/\varepsilon_{xx}$, while comparing the strains in the x- and y-directions provides an equivalent Poisson's ratio $v_0^* = -\varepsilon_{yy}/\varepsilon_{xx}$. Table 1 shows numerical values for $w = 100$ nm and combinations of L and F giving similar strains. E_0^* varies considerably, while v_0^* tends to unity as w/L decreases.

These values may be compared with predictions made by ignoring axial displacements and assuming each member deflects as a clamped-guided beam, which yield $E_0^*/E_{45} = 2(w/L)^3$ and $v_0^* = 1$ [7]. There is good agreement, suggesting that analytic approximations suffice when bending dominates and provide simple scaling laws. Thus, structuring reduces the effective Young's modulus by a large, geometrically controllable factor. However, values of E^* and ν^* are entirely different for loads at 45° (≈w/L and zero, respectively) so the material is anisotropic.

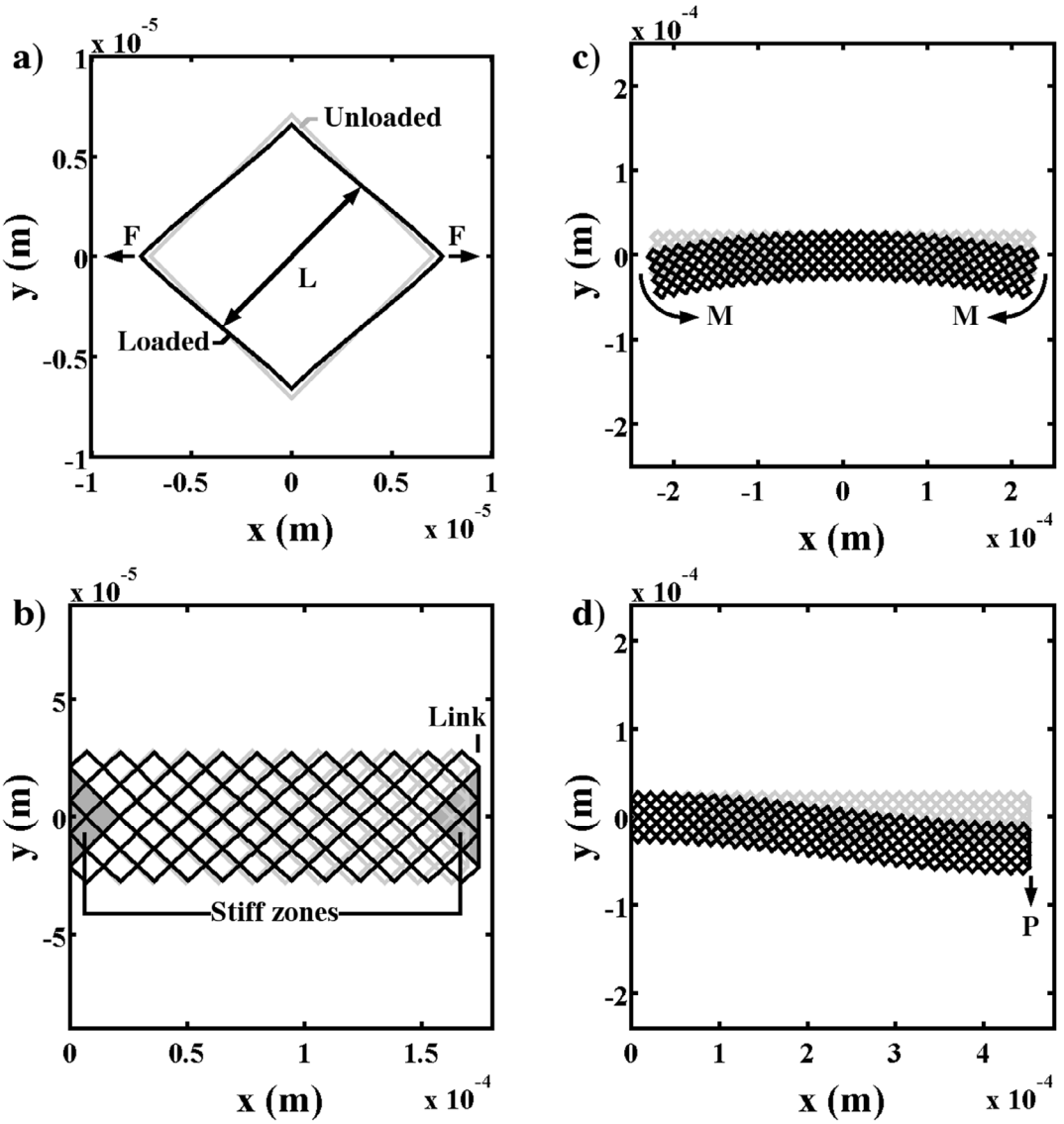

Figure 3. Deflections of diamond cellular material: (a) single cell and (b) 4 × 12 array under tension; (c) 4 × 32 array under pure bending; (d) 4 × 32 array under clamped-guided bending.

2.5. Brittle fracture

The maximum strain of each member is $\varepsilon_{\max} = w/2R$, where $1/R = M/E_{45}I$ is the curvature and M is the maximum bending moment. For a clamped-guided member with a transverse load P, this occurs at each end and has the value $M = PL/2$. From the corresponding transverse deflection ($u_{y\max} = PL^3/12E_{45}I$) we obtain $1/R = 6u_{y\max}/L^2$, or $6\varepsilon_0^*/L$ where ε_0^* is the effective strain of the cell. Assuming each member fails at a strain ε_{f45}, the effective fracture strain is $\varepsilon_{f0}^*/\varepsilon_{f45} = L/3w$. Since $w \ll L$, allowable strains are increased, implying the possibility of long-travel suspensions. However, structuring must be achieved without creating stress-concentrating notches.

2.6. Edge effects

As is well known, this model no longer suffices when cells are constrained. In devices, cellular materials are likely be used locally, connecting to conventional parts at anchors and links. Stresses providing appreciable strains in cellular material will then be so low that boundary displacements must be zero. In this case, the effect of a non-zero v_0^* provides a local constraint, preventing the correct value of E_0^* from being achieved near constrained edges. For example, figure 3(b) shows the deflection of a 4 × 12 sheet of IA material due to horizontal tensile forces of $F = 0.5 \times 10^{-6}$ N per node. The sheet is built-in at the LHS, while the nodes at the RHS are connected with a rigid link. The assumed parameters are $L = 10$ μm, $w = 100$ nm, $d = 4$ μm and $F = 10^{-7}$ N. The non-zero value of v_0^* implies that nodes near the boundary cannot deflect, except through minimal changes in axial length. As a result, there is a stiff transition zone near each end, where estimates based on E_0^* will be incorrect. To quantify this, figure 4(a) shows the variation with aspect ratio of the average value of E_0^* for sheets of different width. The average tends to the analytic value as the aspect ratio rises, although convergence is slower for wider sheets. Effective medium theory is only accurate when edge effects are small.

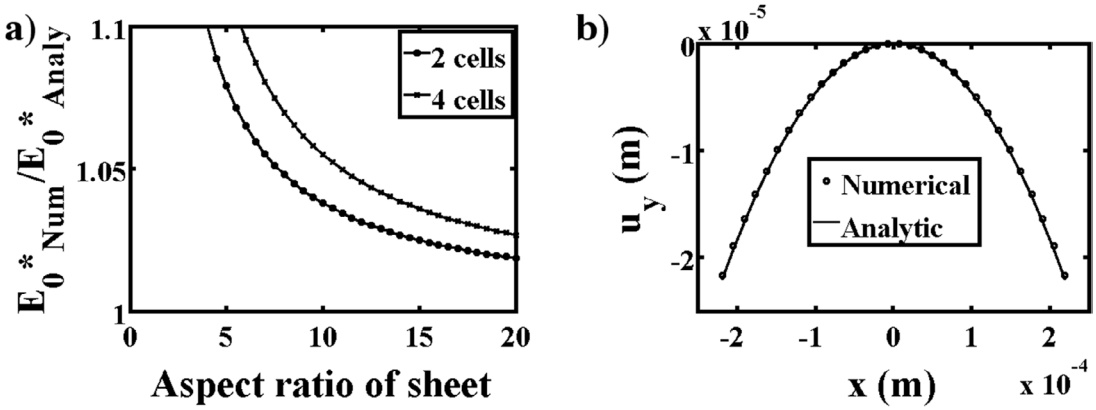

Figure 4. (a) Variation of the average value of E_0^* with aspect ratio, for two sheet widths; (b) numerical and analytic predictions for the deflection of a 4-cell wide beam under pure bending.

2.7. Bending

Pure bending may be simulated using linearly varying loads at end nodes to mimic a moment M. Figure 3(c) shows the deflection of a IA beam with 4×32 cells, assuming $M = 1.414 \times 10^{-11}$ N m. Ignoring axial deflections again, it is simple to obtain the curvature as $1/R = M/E_{45}^* I^*$. Here $I^* = dw^{*3}/12$ is the effective second moment of area and w^* is the effective beam width. For an N-cell wide beam, $(N^3 + N^2/2 - 5N/2 + 1)(L\sqrt{2})^3$ is an approximation for w^{*3}, with w^* tending to the actual width $NL\sqrt{2}$ when N is large. Figure 4(b) compares the midline deflection u_y with the analytic variation; the agreement is remarkable. Provided edge effects are small, effective medium theory should allow deflection to be predicted using standard expressions. Figure 3(c) shows the deflection of a 4×32 IA beam in the clamped-guided configuration due to a total load $P = 8 \times 10^{-8}$ N. Away from the ends, the midline deflection u_y is close to the sigmoidal curve $u_y(x) = x^2(3L_B - 2x)\ (P/12E_{45}^* I^*)$, where x is horizontal position and L_B is beam length. However, there is no bending in the stiff zones.

2.8. Comparative performance

We now compare the lattices highlighted in figure 1. We assume that all flexible members have length L. We also assume initially that the stiff members in the IIA and IIB lattices are inflexible, and that both their unit cells must be elongated in the x-direction by a factor f to allow gaps for motion. Their effective parameters can again be found by assuming that bending dominates and are given in table 2 for uniaxial loads. The lattices exhibit a range of v_0^*, from positive to negative and including zero. Since the cell density is reduced in the x-direction in Type II lattices, E_0^* is increased in each case, and v_0^* is also altered for IIA.

Other differences can be expected at edges. To illustrate this, figure 5 shows deflections the ends of beams formed in each lattice. Here, rigid end links are again used, all members have $d = 4\ \mu$m, flexible members have $L = 10\ \mu$m, $w = 100$ nm, and stiff members have $w = 1\ \mu$m; however, all members are drawn with the same width for clarity. The factor f for IIA and IIB cells is 2.5. The IA beam contains 12×60 cells,

Table 2. Effective medium parameters for the four lattices highlighted in figure 1.

Type	IA	IB	IIA	IIB
E_0^*/E_{45}	$2(w/L)^3$	$(w/L)^3$	$2f(w/L)^3$	$2f(w/L)^3$
v_0^*	1	0.5	$-f$	0

while the IB, IIA and IIB have 6×30, 12×24 and 6×24 cells, respectively. As a result, all beams have the same width ($12 \times 10 \times \sqrt{2} \approx 170\ \mu$m) and length ($60 \times 10 \times \sqrt{2} \approx 850\ \mu$m). Loads are applied to yield an extension of 30 μm, i.e. a strain of 3.5%. In each case, there are edge effects, which increase with $|v_0^*|$. For the IA diamond lattice (a), there is a larger triangular stiff zone. For the IB defected diamond lattice (b), the transition from free to constrained cells is both smoother and faster. For the IIA NPR lattice (c), horizontal members are forced to rotate in the transition region, implying the possibility of large local strains in wide sheets. Only the IIB ZPR lattice (d) purely stretches. However, not all lattices have such short transitions. For example, if the NPR cells in figure 5(c) are rotated through 90°, clamping at the ends provides a strong constraint, preventing transverse expansion and stiffening the entire sheet. Effective medium theory must therefore be used with caution.

3. Cellular materials by STL NEMS processing

In this section, we consider the application of STL to cellular material and the incorporation of such materials in complete NEMS.

3.1. Sidewall transfer lithography

Figure 6(a) shows our patterning process [60], which uses multiple STL cycles to allow intersecting features. Here a 3-mask process is assumed. In step 1, photolithography (PL) and reactive ion etching (RIE) are used to pattern a Si substrate with polygonal features on STL Mask 1, as a set of shallow mesas. In step 2, the process is repeated using STL Mask 2. In step 3, the mesas are coated with a layer, whose horizontal surfaces

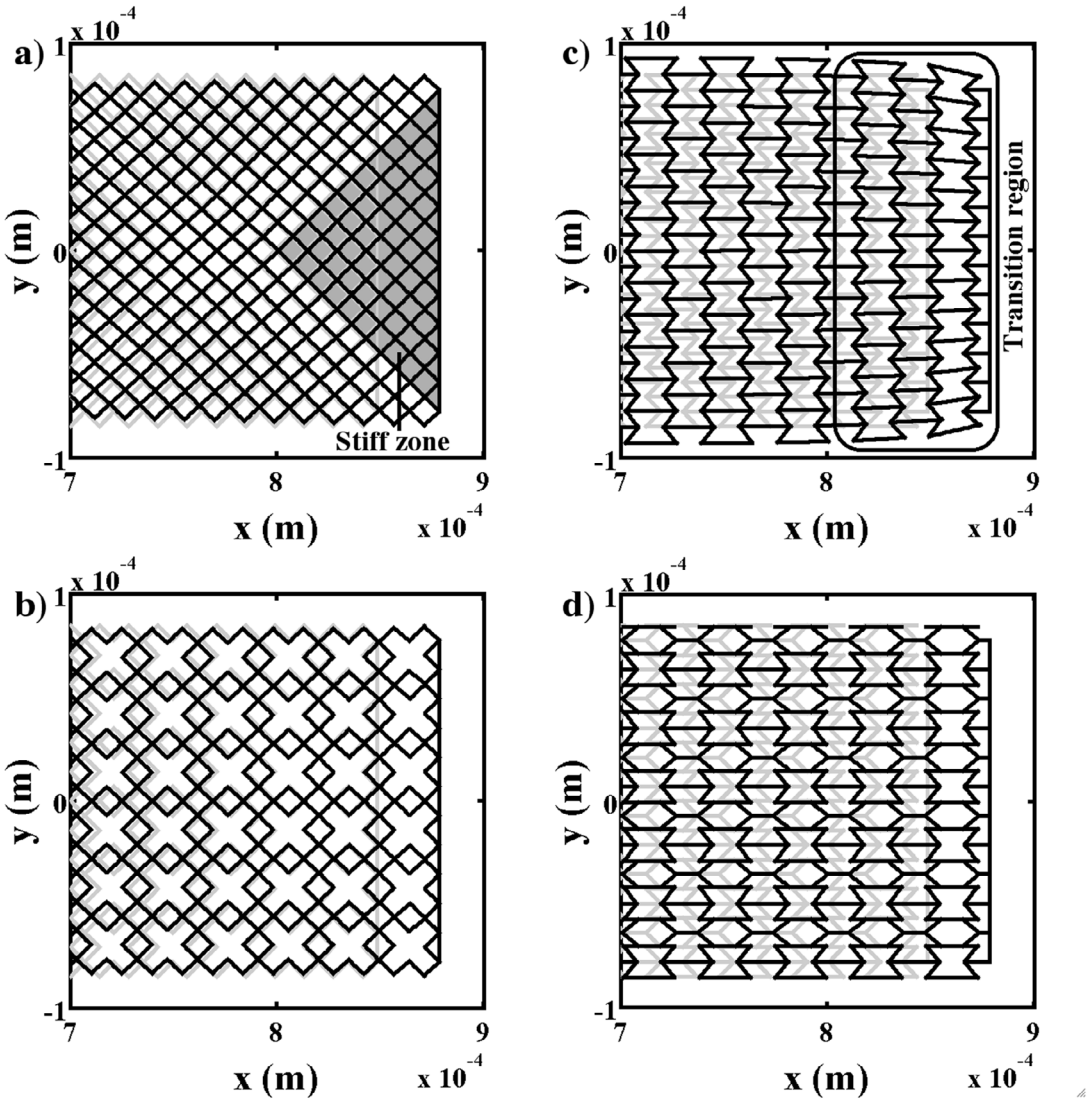

Figure 5. End deflections for stretched beams formed from (a) IA, (b) IB, (c) IIA and (d) IIB lattices.

are discarded to leave the vertical edges as a nanoscale mask. In step 4, PL is used to form microscale patterns in resist. In Step 5, micro- and nano-scale features are transferred together into the substrate. Undercut is then used to form suspended NEMS. Figure 6(b) shows how STL may be used to form the four lattices. Types IA and IB require two levels of STL, using overlaid rectangular and diamond features, respectively. For these lattices, exact periodicity is lost at array edges, since the overlaid STL patterns do not correspond exactly to unit cells. However, for large arrays the effects will be small. IIA and IIB require one level of STL to form accordion-shaped features and one level of PL to form microscale strips. All four lattices can be formed on a single wafer.

Figure 7(a) shows our BSOI NEMS process. The two STL steps involve patterning and etching a first set of mesas (steps 1–3), and then patterning and etching a second set (4, 5). STL processes have used polysilicon [48], Si_3N_4 [49], SiO_2 [53] or metal [51] masks. We have used gold, which has low intrinsic stress and a high selectivity to Si during DRIE, but which also requires a thin interlayer such as Cr to improve adhesion. However, if Au is inappropriate, low-stress PECVD oxide is a useful alternative. A semi-conformal coating (i.e. a coating that at least preserves the angular topology of the surface) is deposited (6), and its horizontal surfaces removed by directional etching (7). The result is a surface mask defining overlaid nanoscale features. PL is then used to add microscale parts (8) and the combined pattern is transferred into the substrate by DRIE (9, 10). Suspended parts are freed by etching away sacrificial oxide (11) and Al is deposited to allow electrical contact (12). So far, the sidewall mask has been left in place, without apparently effecting mechanical response [59].

The lattices were formed with periods and sheet sizes corresponding to the simulations of figure 5. However, the stiff horizontal beams in IIA and IIB cells were widened to 3 μm to increase alignment tolerance. To accommodate this, the flexible diagonal members were made longer and arranged as the hypotenuse of a 3-4-5 triangle rather than at 45°. The effect was to reduce f to 1.75 and alter the member angle to $\theta = \tan^{-1}(4/3)$, reducing the expected value of v_0^* for IIA to $-f\cot(\theta) = -1.3125$. The sheets were combined with micro-scale anchors, using overlap to ensure attachment. Link beams and pull rods were incorporated for actuation in the

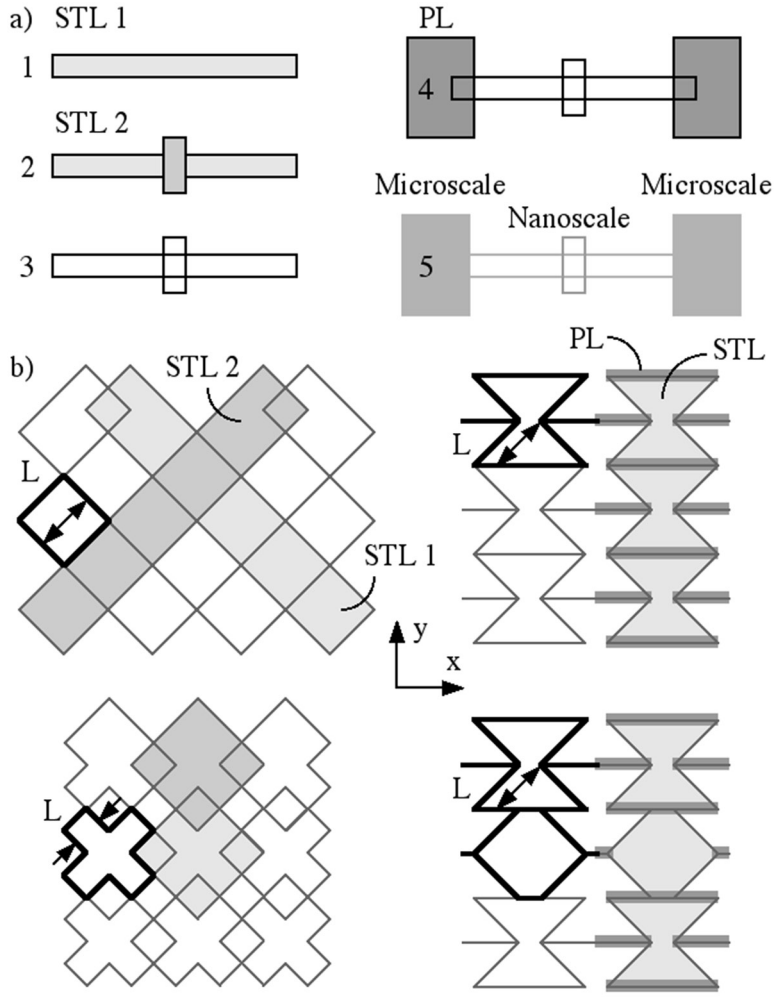

Figure 6. (a) Patterning in a STL NEMS process; (b) patterns needed for IA, IB, IIA and IIB lattices.

axial and transverse direction as shown in figure 7(b), with latches for fixing.

3.2. Device fabrication

Patterns were defined using laser-written masks with a minimum feature size of 1.5 μm. Devices were fabricated in 100 mm diameter (1 0 0) BSOI wafers with a 5 μm device layer and a 2 μm oxide layer. Process details are similar to those in [60]. Patterning was carried out using a mid-UV contact aligner. A 0.4 μm thick layer of Shipley S1805 resist was used for STL 1, while 1.5 μm of Shipley S1813 was used for STL 2 and to define microscale parts. Mesas were etched to a depth of 0.4 μm using a STS DRIE system, using a cyclic process based on SF_6 and C_4F_8 [61]. The shallowest members were therefore $\approx$4 μm deep. Metal deposition and etching were carried out using a RF sputter coater. 100 nm Au was first deposited, using 10 nm Cr for adhesion, and horizontal layers were sputtered away in Ar gas. Material was deposited at high pressure (1.5×10^{-2} mbar) and sputter-etched at relatively low pressure (2×10^{-3} mbar). To reduce intrinsic stress further, both processes were carried out at a low enough power (100 W) to maintain a low temperature. Etching and passivation were adjusted during DRIE to hold the member width close to 100 nm. The main problem was the formation of silicon grass from resputtered Cr. However, this was again avoided with careful process control. Suspended parts were undercut using HF vapour, and Al metallisation deposited by thermal evaporation. Structures released without obvious stress-induced distortions.

Structures were evaluated by scanning electron microscopy (SEM) and optical surface profilometry. Figure 8 shows SEM views during processing [60]. Figure 8(a) shows a two-layer mesa, in the criss-cross pattern needed for IA material. Figure 8(b) shows Au metal over a mesa edge, before sputter etching to form the sidewall mask. To highlight the metal, the mesa has been oxidized before coating, and dipped in HF after cleaving. The metal is thinner on vertical surfaces but coverage is continuous. Figure 8(c) shows the completed mask. There are small height differences between the metal in the two STL layers; these do not affect pattern transfer. Figure 8(d) shows the structure after DRIE; the sidewall mask has been transferred into high aspect ratio Si sheets. Orthogonal features have similar widths; however, a small height variation (one mesa depth) can be seen. For deep structures, this will have minimal mechanical effect. Figures 9(a)–(d) shows surface profiles of IA, IB, IIA and IIB masks, which correspond

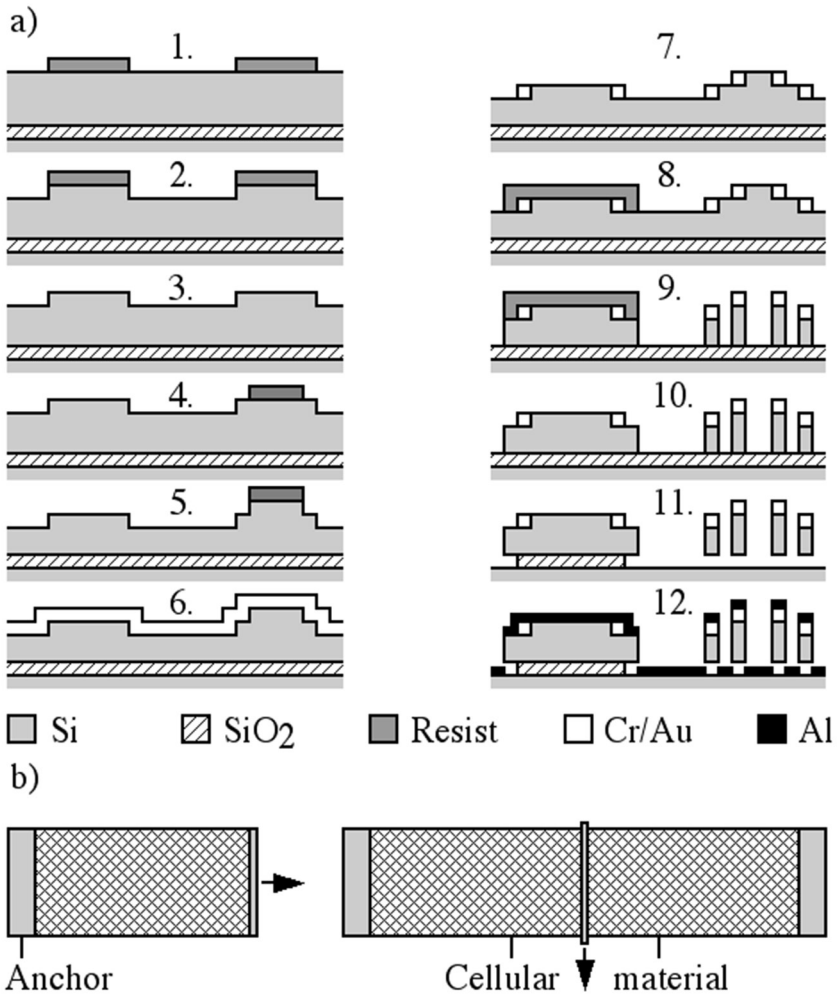

Figure 7. STL NEMS fabrication process; (b) generic NEMS containing embedded cellular materials.

to figure 6(b). Figures 10(a)–(d) shows SEM views of the four suspended lattices. As discussed earlier, periodicity is lost at free edges for IA and IB materials. Other imperfections include corner rounding, changes in mark-to space ratio and overlay errors. Improved results could easily be obtained using deep UV lithography. Figure 10(e) shows a transverse pull-rod with IA material and figure 10(f) an axial pull-rod with IIA material. The materials are highly flexible, and can easily be bent out-of-plane, as shown in figures 10(g) and (h).

4. Mechanical testing

The combination of large suspended structures and small features complicated metrology. For example, small movements were observed during SEM inspection, due to charging or heating. Even though the flexible members are visible in optical microscopes, they cannot properly be resolved, or visualised in detail except over a small field of view, and background lightening was required to clarify some photographs.

4.1. Tensile testing

Mechanical testing was carried out under a microscope, using a probe-tip for actuation. Figure 11(a) shows the arrangement for stretching a IA beam through a fixed distance of 30 μm, corresponding to a strain of $\approx$3.6%. Figures 11(b)–(e) show microscope views of the ends of beams in the four different lattices when subject to this strain, which should be compared with figure 5. All show edge effects at the boundary between the cellular material and the rigid link used to apply loads. For the IA lattice (b), the transition region can be identified from the change in slope of diagonal members. No such abrupt change can be seen in the IB lattice (c), although distortion of the unit cell can be measured directly from comparative photographs with the lattice relaxed. For the IIA lattice (d), rotation of the stiff horizontal members can be seen in the transition region. However, for the IIB lattice (e), these members remain horizontal. To illustrate the effect of orientation, figure 11(f) shows the end of a strained beam formed using IIA cells that have been rotated through 90°. Although auxetic behaviour might again be expected, the strong constraint on the stiff members has prevented transverse expansion, as mentioned previously. v_0^* was estimated from the average longitudinal strain (3.5%) and the transverse strain away from the transition region. The following results were obtained. IA: $v_0^* = +0.86$ (predicted value +1); IB: $v_0^* = +0.48$ (+0.5); IIA: $v_0^* = -1.21$ (-1.3125) and IIB: $v_0^* = 0$ (as expected). Non-zero values are within reasonable experimental error.

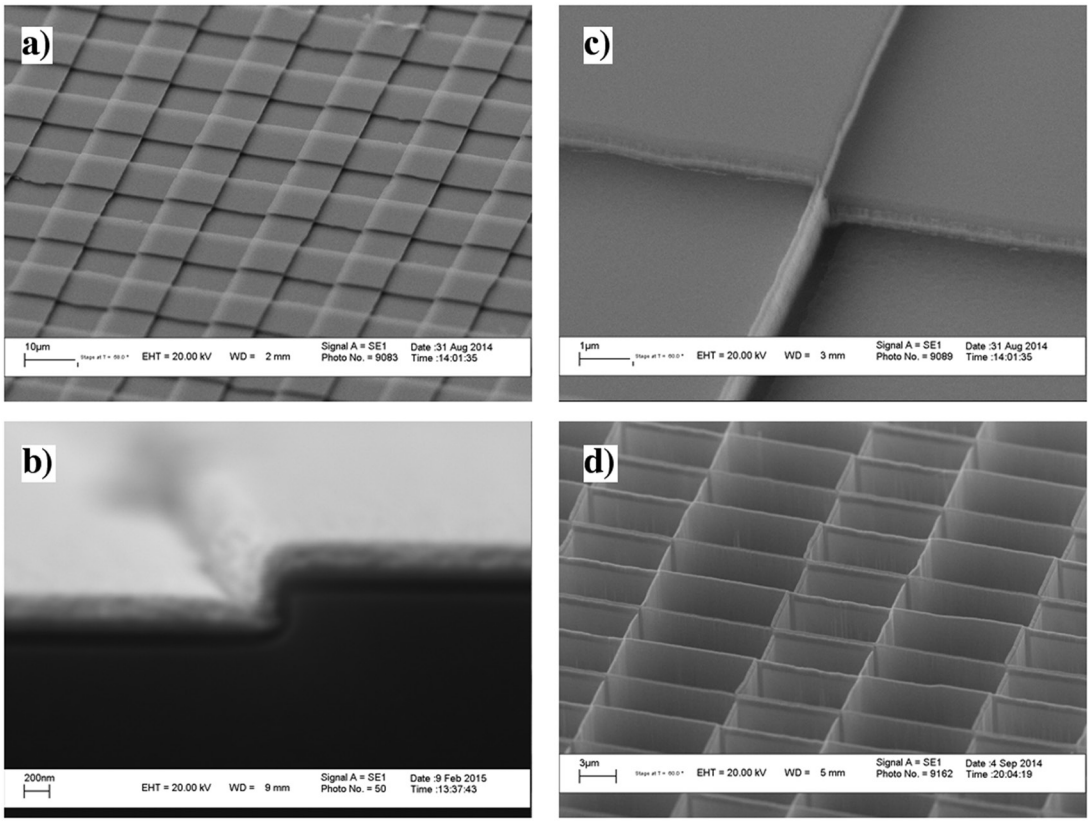

Figure 8. SEM views of IA lattices at different stages in fabrication: (a) overlaid mesa structure; (b) metal-coated mesa, (c) completed sidewall mask, and (d) etched silicon structure. (a), (c), and (d) © [2015] IEEE. Reprinted, with permission, from [60].

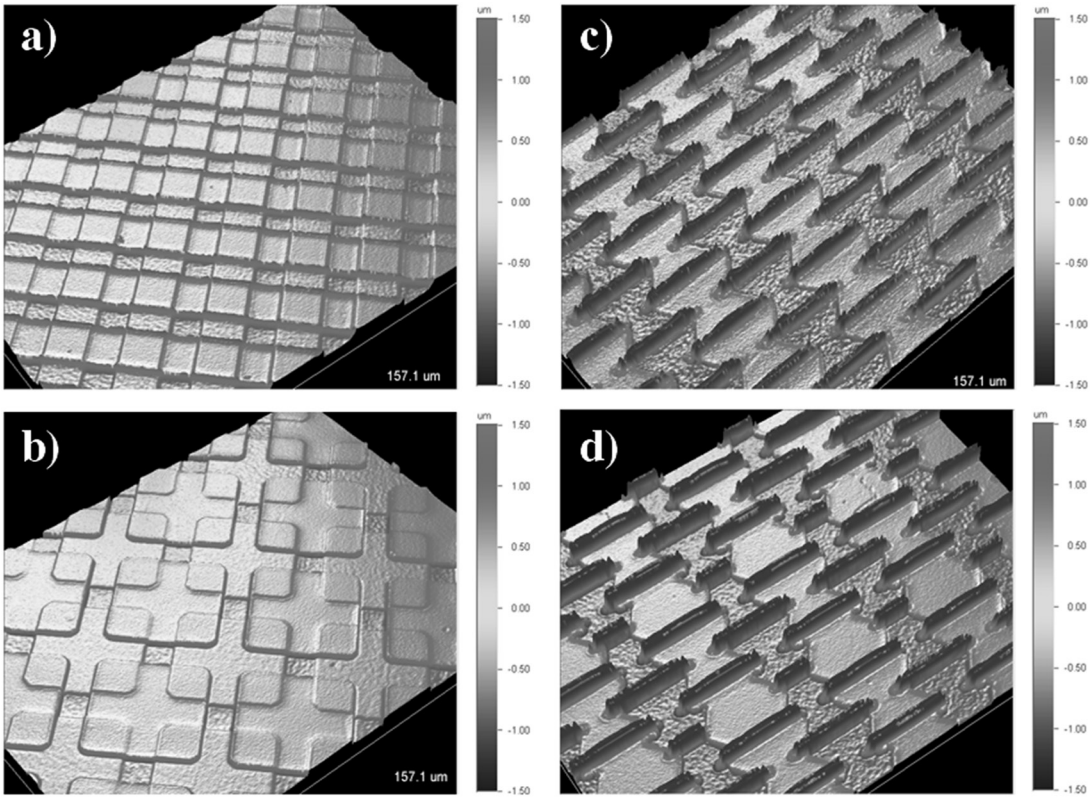

Figure 9. Surface profiles of (a) IA, (b) IB, (c) IIA and (d) IIB lattices, after mask formation.

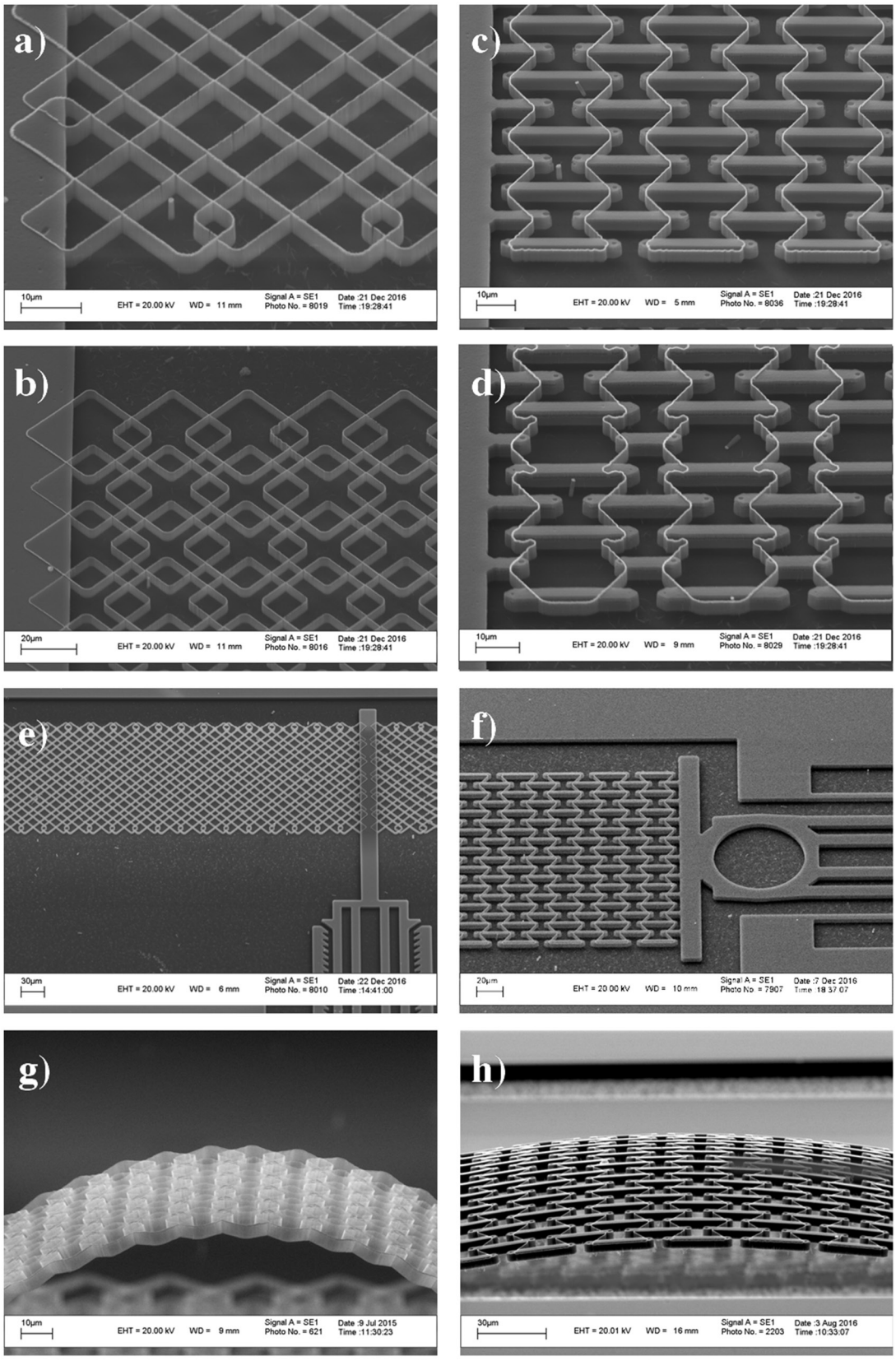

Figure 10. SEM views of (a) IA, (b) IB, (c) IIA and (d) IIB lattices; completed NEMS designed for (e) transverse and (f) axial deflection; (g) and (h) IB and (b) IIA lattices after buckling out-of-plane.

4.2. Electrostatic actuation

Elastic coefficients can in principle be determined from axial deflections applied by an actuator such as an electrostatic comb-drive. However, stress-induced misalignment complicates measurement. We therefore present results only for a single lattice of Type IB as shown in figure 12(a). Here a wider sheet contained 18 × 16 cells was used, while the comb

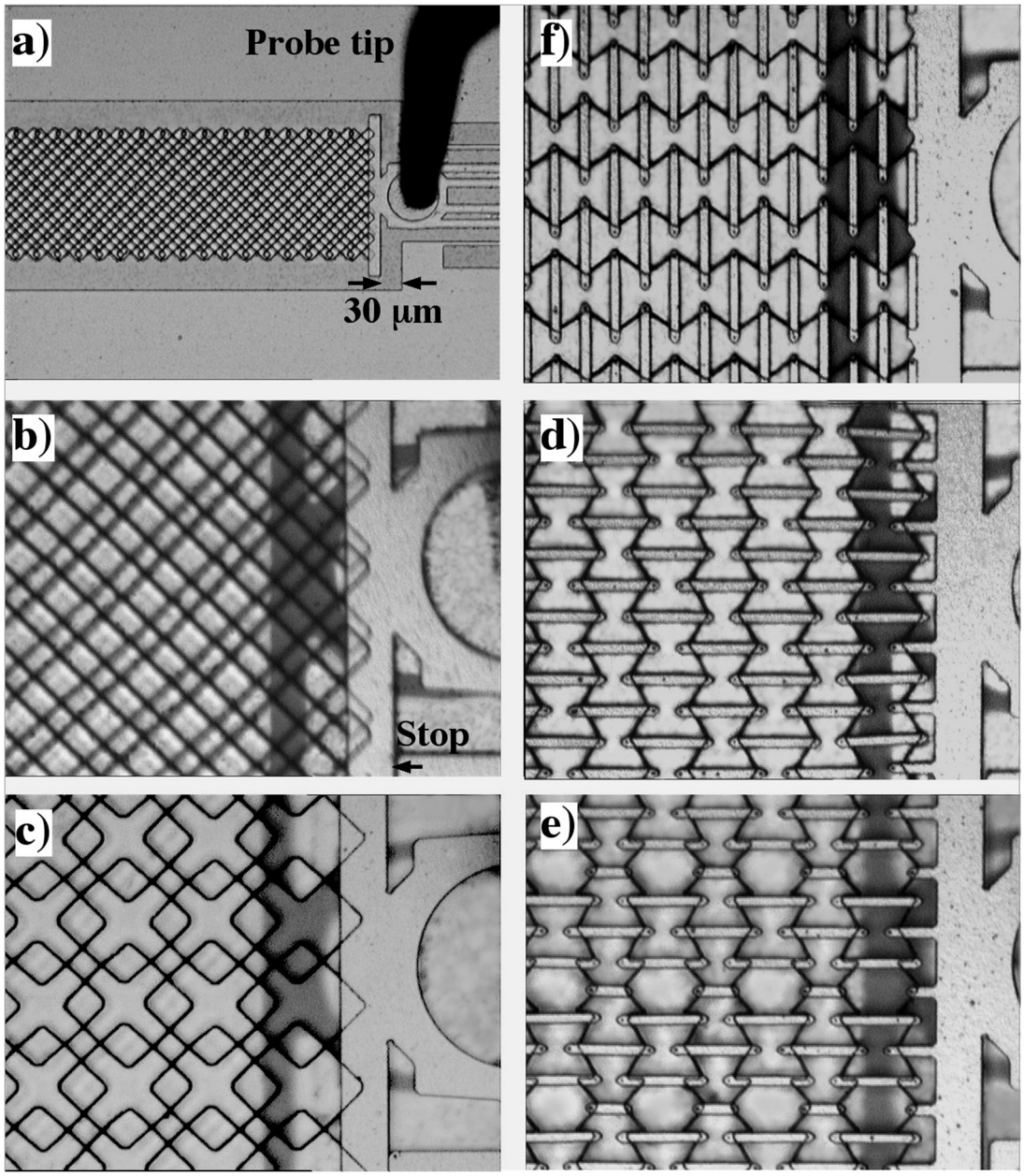

Figure 11. Optical views of (a) arrangement for tensile testing, and strained lattices containing (b) IA, (c) IB, (d) IIA, (e) IIB and (f) IIA lattices with cells rotated by 90°.

contained 48 electrode gaps, each measuring 5 μm. *A* voltage V was applied between the anchors, with the fixed beam end and substrate grounded. The circles in figure 12(b) show the variation of in-plane (x) deflection with V^2, while the crosses show the out-of-plane (z) height of the moving comb above the fixed comb. The x-deflection initially increases rapidly, and then follows a linear characteristic with lower slope. The z-deflection is initially positive, but then gradually reduces.

The initial response can be explained by electrode misalignment caused by out-of-plane curvature, since improvements to alignment caused by flattening the sheet will lead to a large deflection at low force. The final response can be explained using the standard model of a comb actuator. The force due to an actuator with variable capacitance $C(x)$ is $F = 1/2\ \mathrm{d}C/\mathrm{d}x\ V^2$. For a comb-drive with N electrode gaps g, $\mathrm{d}C/\mathrm{d}x = N\varepsilon_0 d/g$. If the beam has axial stiffness k_T, it will deflect until the spring force $k_T\Delta x$ balances the electrostatic force, so $\Delta x = (N\varepsilon_0 d/2k_T g)V^2$. The stiffness of a single cell is $k = E_0^* d$, or $E_{45}d(w/L)^3$ for Type IB material (table 2). Here, $k \approx 130 \times 10^9 \times 4 \times 10^{-6} \times (0.1/10)^3 = 0.52\,\mathrm{N\,m^{-1}}$. Ignoring boundary effects, the stiffness of a beam with 16 cells in parallel and 18 in series is $k_T \approx 0.52 \times 16/18 = 0.46\,\mathrm{N\ m^{-1}}$. Consequently, $\Delta x \approx 48 \times 8.85 \times 10^{-12} \times 4/(2 \times 0.46 \times 5)\ V^2\ (\mathrm{m}) = 0.37 \times 10^{-3}\ V^2\ (\mu\mathrm{m})$. The dashed line in figure 12(b) shows the prediction of this model, assuming an offset of 2.7 μm to account for misalignment. There is reasonable agreement with the data, confirming the earlier estimate for elastic properties.

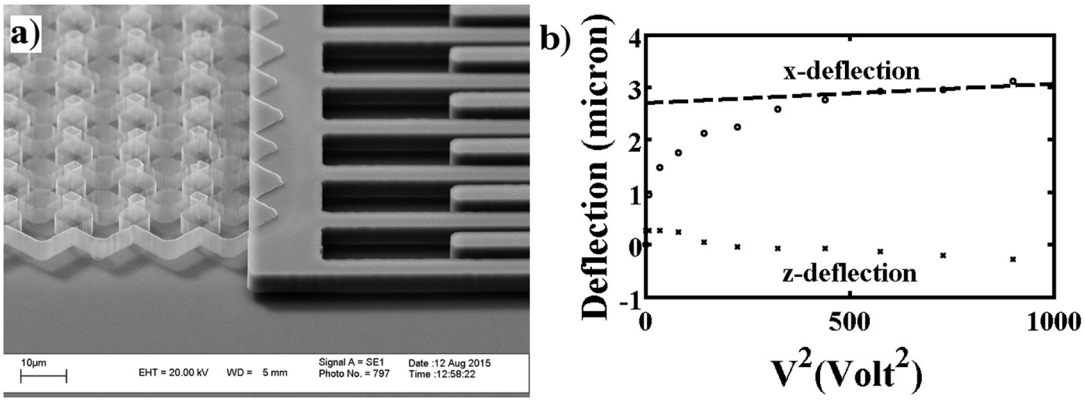

Figure 12. (a) SEM view of a type 1B sheet with an electrostatic comb actuator; (b) comparison between experimental and theoretical deflection characteristics.

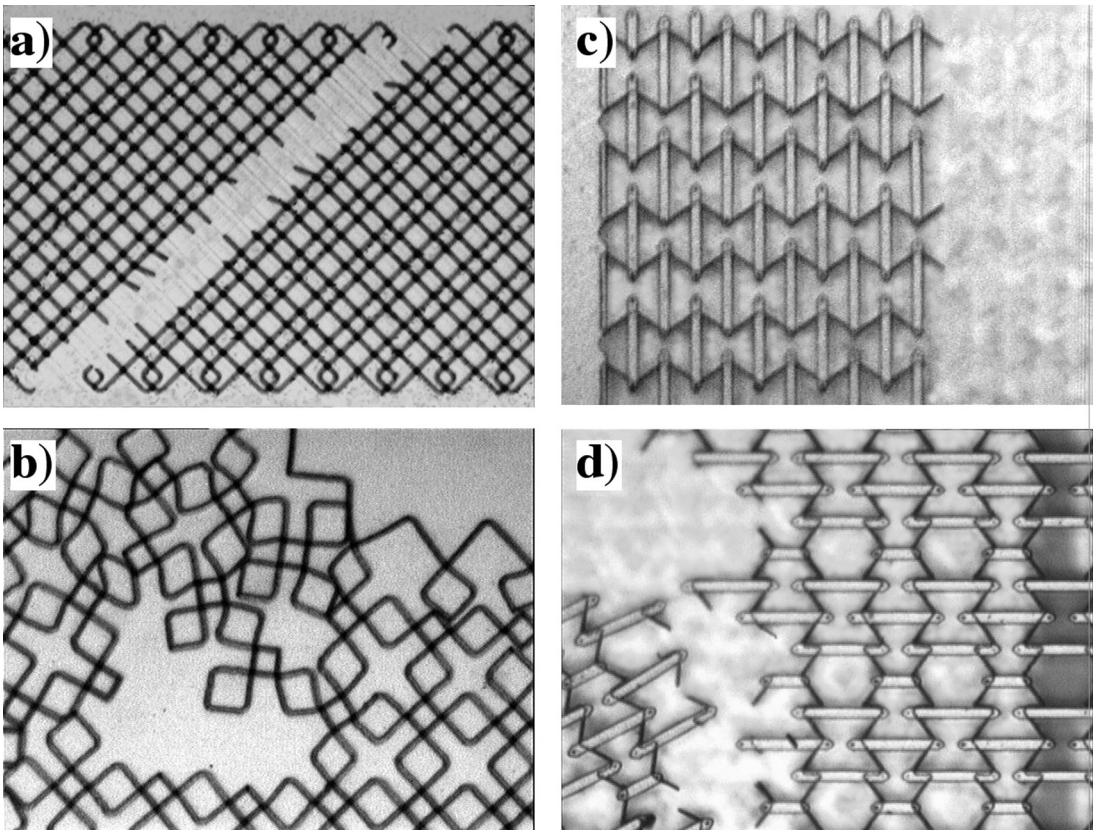

Figure 13. Optical views of fractured lattices: (a) IA, (b) IB, (c) IIA and (d) IIB.

4.3. Brittle fracture

Higher strains were applied in dies without end-stops. Insufficient devices were fabricated to allow statistics; however, characteristic failure modes were still identified. Type IA lattices mainly failed through diagonal fracture as shown in figure 13(a). Crack propagation appeared to follow models in which failure of one member causes a notch in the cellular sheet that transfers additional stress to adjacent members [21]. The nanoscale stubs decorating the separated edges are generally full-length, implying that members have mainly broken at the point of maximum moment rather than at stress concentrations induced by surface notches. Cracks in Type IB lattices did not propagate, but caused open tears with large accompanying distortion (figure 13(b)). Type IIA lattices mainly cleaved at right angles to the beam axis, especially when rotated by 90° (figure 13(c)), while IIB failed along more wandering perpendicular loci (figure 13(d)).

4.4. Bending

Clamped-guided bending was achieved by applying transverse deflections at beam centres. However, it was difficult to image the entirety of such large structures with precision. Figure 14(a) shows an optical view of a IA beam after latching into position. The deflected shape broadly follows the sigmoidal curve expected from figure 3(d). However, the increased beam width has resulted in larger stiff zone. To highlight this, figure 14(b)

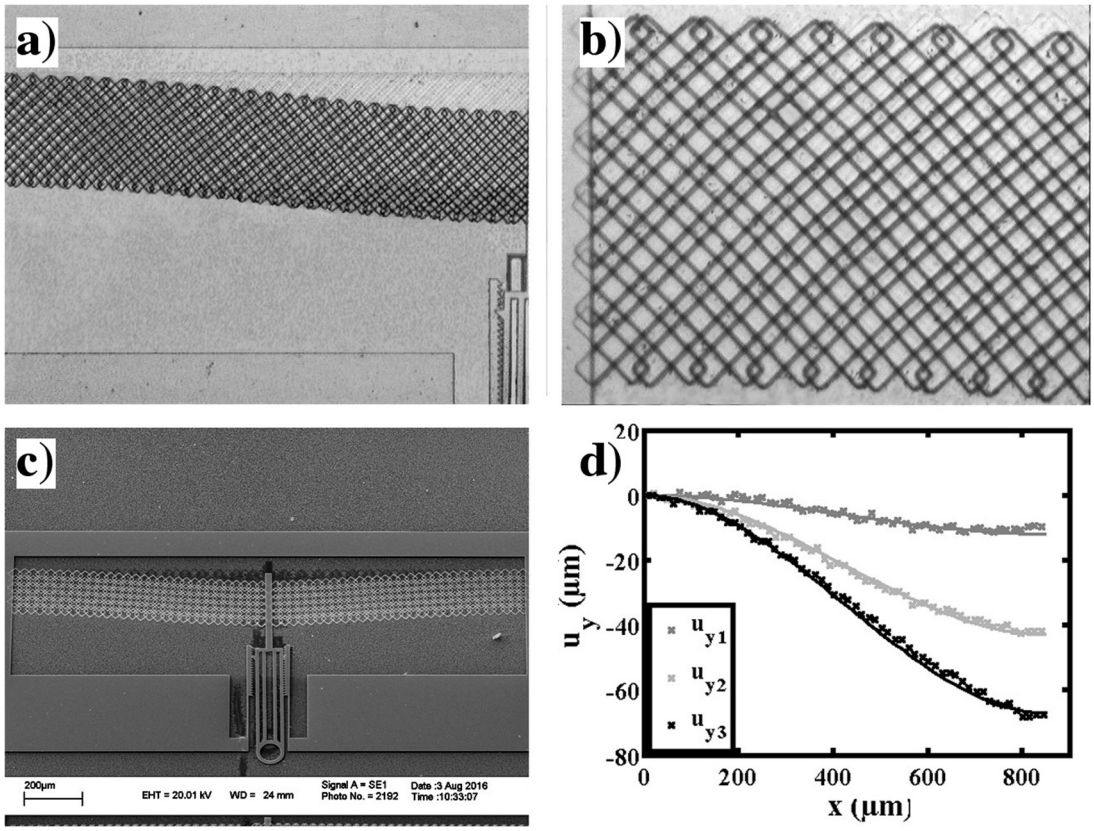

Figure 14. (a) and (b) Optical views of IA lattice after bending; (c) SEM view of IB lattice after bending; (d) experimental and theoretical beam profiles for different deflections.

shows an enlarged view near the anchor, where the stiff zone may again be identified from the change in slope of flexible members. Figure 14(c) shows a SEM view of a IIA beam (which has reduced edge effects) after latching into position. Figure 14(d) compares experimental midline profile of the loaded beam with the expected sigmoidal curve, for three different peak deflections. There is generally good agreement, although this degrades as the deflection rises. Brittle failure during bending generally occurred at beam-ends, where the effective bending moment is largest. Mechanical behaviour therefore broadly corresponds to theoretical predictions.

5. Conclusions

We have shown that sidewall transfer lithography and deep reactive ion etching provide a practical method of fabricating nanostructured 2D cellular material with well-controlled feature size at low cost. No electron-beam lithography is required, simply the addition of two optical lithography cycles and some conventional surface processing. We have fabricated NEMS containing cellular materials and used them to investigate stretching, bending and brittle fracture. Mechanical behaviour largely follows theoretical predictions made using the stiffness matrix method. However, modelling and experiment both highlight the need to control Poisson's ratio to avoid edge effects. There is considerable scope to develop alternative unit cells to explore anisotropy or control non-linearity. Example applications include mechanical devices requiring long travel or low resonant frequency. However, since the structuring must also control thermal conductivity, there may also be applications in thermal MEMS. Process development is clearly required to improve lithography, reduce overlay errors, reduce cell size and increase feature height. Further work is also required to determine repeatability and reliability. However, the STL approach represents a rare example of a foundry compatible NEMS process.

References

[1] Middlehoek S and Audet S 1989 *Silicon Sensors* (New York: Academic)
[2] Senturia S D 2000 *Microsystem Design* (Dordrecht: Kluwer)
[3] Petersen K E 1982 Silicon as a mechanical material *Proc. IEEE* **70** 420–57
[4] Madou M J 1997 *Fundamentals of Microfabrication* (Boca Raton, FL: CRC Press)
[5] Engheta N and Ziolkowski R W 2006 *Metamaterials* (New York: Wiley)
[6] Smith D R, Padilla W J, Vier D C, Nemat-Nasser S C and Schultz S 2000 Composite medium with simultaneously negative permeability and permittivity *Phys. Rev. Lett.* **84** 4184–7
[7] Gibson L J and Ashby M F 1999 *Cellular Solids: Structure and Properties* (Cambridge: Cambridge University Press)
[8] Christensen R M 2000 Mechanics of cellular and other low-density materials *Int. J. Solids Struct.* **37** 93–104
[9] Gibson L J, Ashby M F, Schajer G S and Robertson C I 1982 The mechanics of two-dimensional cellular materials *Proc. R. Soc. Lond.* A **382** 25–42

[10] Gibson L J and Ashby M F 1982 The mechanics of three-dimensional cellular materials *Proc. R. Soc. Lond.* A **382** 43–59
[11] Silva M J, Hayes W C and Gibson L J 1995 The effects of non-periodic microstructure on the elastic properties of two-dimensional cellular solids *Int. J. Mech. Sci.* **37** 1161–77
[12] Gibson L J 2000 Mechanical behaviour of metallic foams *Ann. Rev. Mater. Sci.* **30** 191–227
[13] Hyun S and Torquato S 2002 Optimal and manufacturable two-dimensional, Kagomé-like cellular solids *J. Mater. Res.* **17** 137–44
[14] Kim H S and Al-Hassani S T S 2003 Effective elastic constants of two-dimensional cellular materials with deep and thick cell walls *Int. J. Mech. Sci.* **45** 1999–2016
[15] Wang A-J and McDowell D L 2004 In-plane stiffness and yield strength of periodic metal honeycombs *J. Eng. Mater. Technol.* **126** 137–56
[16] Tuncer E 2005 Numerical calculations of effective elastic properties of two cellular structures *J. Phys. D: Appl. Phys.* **38** 497–503
[17] Zhang Y H, Qiu X M and Fang D N 2008 Mechanical properties of two novel planar lattice structures *Int. J. Solids Struct.* **45** 3751–68
[18] Maiti S K, Ashby M F and Gibson L J 1984 Fracture toughness of brittle cellular solids *Scr. Metall.* **18** 213–7
[19] Zhang J and Ashby M F 1992 Buckling of honeycombs under in-plane biaxial stresses *Int. J. Mech. Sci.* **34** 491–509
[20] Quintana Alonso I and Fleck N A 2007 Damage tolerance of an elastic-brittle diamond-celled honeycomb *Scr. Mater.* **56** 693–6
[21] Lipperman F, Rykin M and Fuchs M B 2007 Nucleation of cracks in two-dimensional periodic cellular material *Comput. Mech.* **39** 127–39
[22] Srikantha Phani A, Woodhouse J and Fleck N A 2006 Wave propagation through two-dimensional periodic lattices *J. Acoust. Soc. Am.* **119** 1995–2005
[23] Gonella S and Ruzzene M 2008 Analysis of in-plane wave propagation in hexagonal and re-entrant lattices *J. Sound Vib.* **312** 125–39
[24] Almgren R F 1985 An isotropic three-dimensional structure with Poisson's ratio −1 *J. Elast.* **15** 427–30
[25] Evans K E 1989 Tensile network microstructures exhibiting negative Poisson's ratios *J. Phys. D: Appl. Phys.* **22** 1870–6
[26] Ohtaki H, Hu G, Nagasaka Y and Kotosaka S 2004 Analysis of negative Poisson's ratios of re-entrant honeycombs *JSME Int. J.* A **47** 113–21
[27] Attard D and Grima J N 2011 Modelling of hexagonal honeycombs exhibiting zero Poisson's ratio *Phys. Status Solidi* **1** 52–9
[28] Torquato S, Gibiansky L V, Silva M J and Gibson L J 1998 Effective mechanical and transport properties of cellular solids *Int. J. Mech. Sci.* **40** 71–82
[29] Lakes R 2007 Cellular solids with tunable positive or negative thermal expansion of unbounded magnitude *Appl. Phys. Lett.* **90** 221905
[30] Wadley H N G 2002 Cellular metals manufacturing *Adv. Eng. Mater.* **4** 726–33
[31] Banhart J 2001 Manufacture, characterisation and application of cellular metals and metal foams *Prog. Mater. Sci.* **46** 559–632
[32] Gibson L J 2005 Biomechanics of cellular solids *J. Biomech.* **38** 377–99
[33] Li L and Sottos N R 1995 Improving hydrostatic performance of 1–3 piezocomposites *J. Appl. Phys.* **77** 4595–603
[34] Smith W A 2002 Modeling 1–3 composite piezoelectrics: hydrostatic response *IEEE Trans. Ultrason. Ferroelectr. Freq. Control* **40** 41–9
[35] Rottenberg X, Jansen R, Van Hoof C and Tilmans H A C 2011 Acoustic metamaterials in MEMS BAW resonators *Appl. Phys.* A **103** 869–75
[36] Kachroudi A, Basrour S, Rufer L and Jomni F 2015 Piezoelectric cellular micro-structured PDMS material for micro-sensors and energy harvesting *J. Phys.: Conf. Ser.* **660** 012040
[37] Larsen U D, Sigmund O and Bouwstra S 1997 Design and fabrication of compliant micro-mechanisms and structures with negative Poisson's ratio *J. Microelectromech. Syst.* **6** 99–106
[38] Levy O, Steinberg B Z, Boag A, Krylov S and Goldfarb I 2007 Mechanical tuning of two-dimensional photonic crystal cavity by micro electro mechanical flexures *Sensors Actuators* A **139** 47–52
[39] Levy O, Krylov S and Goldfarb I 2015 Design considerations for negative Poisson's ratio structures under large deflection for MEMS applications *Smart Mater. Struct.* **15** 1459–66
[40] Lee J-H, Singer J P and Thomas E L 2012 Micro-/nanostructured mechanical metamaterials *Adv. Mater.* **24** 4782–810
[41] Xu B, Arias F, Brittain S T, Zhao X M, Gryzbowski B, Torquato S and Whitesides G M 1999 Making negative Poisson's ratio microstructures by soft lithography *Adv. Mater.* **11** 1186–9
[42] Muslija A and Lantada A D 2014 Deep reactive ion etching of auxetic structures: present capabilities and challenges *Smart Mater. Struct.* **23** 087001
[43] Cuisin C *et al* 2000 Sub-micrometer resolution Yablonovite templates fabricated by x-ray lithography *Appl. Phys. Lett.* **77** 770772
[44] Bückmann T *et al* 2012 Tailored 3D mechanical metamaterials made by dip-in direct-laser-writing optical lithography *Adv. Mater.* **24** 2710–4
[45] Zheng X *et al* 2014 Ultralight, ultrastiff mechanical materials *Science* **344** 1373–7
[46] Wang K, Chang Y-H, Chen Y, Zhang C and Wang B 2015 Designable dual-material auxetic metamaterials using three-dimensional printing *Mater. Des.* **67** 159–64
[47] Silverberg J L, Evans A A and McLeod L 2014 Using origami design principles to fold reprogrammable mechanical metamaterials *Science* **345** 647–50
[48] Hunter W R, Holloway T C, Chatterjee P K and Tasch A F 1981 A new edge-defined approach for submicrometer MOSFET fabrication *IEEE Electron. Device Lett.* **2** 4–6
[49] Hilleringmann U, Vierigge T and Horstmann J T 2000 A structure definition technique for 25 nm lines of silicon and related material *Microelectr. Eng.* **53** 569–72
[50] Flanders D C and Efremow N N 1983 Generation of <50 nm period grating using edge defined techniques *J. Vac. Sci. Technol.* B **1** 1105–8
[51] Weber T *et al* 2012 High aspect ratio deep UV wire grid polarizer by double patterning *Microelectr. Eng.* **98** 433–5
[52] Hsu D S Y and Gray H F 1996 Vertical thin-film-edge field emitters: fabrication by chemical beam deposition, imaging of cathodoluminescence and characterisation of emission *Thin Solid Films* **286** 92–7
[53] Choi Y-K, Zhu J, Grunes J, Bokor J and Somorjai G A 2003 Fabrication of sub-10 nm silicon nanowire arrays by size reduction lithography *J. Phys. Chem.* **10** 3340–43
[54] Zhang Z, Lu J, Hellström P-E, Östling M and Zhang S-L 2006 Ni_2Si nanowires of extraordinarily low resistivity *Appl. Phys. Lett.* **88** 213103
[55] Grabiec P B, Zaborowski M, Domanski K, Gotszalk T and Rangelow I W 2004 Nano-width lines using lateral pattern definition technique for nanoimprint template fabrication *Microelectr. Eng.* **73–4** 599–603
[56] Zhao Y, Berenschot E, de Boer M, Jansen H, Tas N, Huskens J and Elwenspoek M 2008 Fabrication of a silicon oxide stamp

by edge lithography reinforced with silicon nitride for nanoimprint lithography *J. Micromech. Microeng.* **18** 064013
[57] Jalabert L, Sato T, Kumemura M, Bolsee D, Hermans C, BenMoussa A and Fujita H 2010 Embedding vertical nanosheets of metals into PDMs with a reusable template engineering *Proc. IEEE MEMS Conf. (24–28 January, Hong Kong)* pp 384–7
[58] Xie Q, Zhou Q, Xie F, Sang J, Wang W, Zhang H A, Wu W and Li Z 2012 Wafer-scale fabrication of high-aspect ratio nanochannels based on edge-lithography technique *Biomicrofluidics* **6** 016502
[59] Liu D and Syms R R A 2014 NEMS by sidewall transfer lithography *J. Microelectromech. Syst.* **23** 1366–73
[60] Liu D and Syms R R A 2015 NEMS by multilayer sidewall transfer lithography *Proc. 28th IEEE MEMS Conf. (18–22 January, Estoril, Portugal)* pp 288–91
[61] Bhardwaj J K and Ashraf H 1995 Advanced silicon etching using high density plasmas *Proc. SPIE* **2639** 224–33
[62] Benitez A, Esteve J and Bausells J 1995 Bulk silicon microelectromechanical devices fabricated from commercial bonded and etched-back silicon-on-insulator substrates *Sensors Actuators* A **50** 99–103
[63] Williams M S and Todd J D 2000 *Structures: Theory and Analysis* (London: Macmillan)
[64] Livesey R K 1964 *Matrix Methods of Structural Analysis* (Oxford: Pergamon)
[65] McGuire W, Gallagher R H and Zieman R D 2000 *Matrix Structural Analysis* 2nd edn (New York: Wiley)
[66] Wortman J J and Evans R A 1965 Young's modulus, shear modulus, and Poisson's ratio in silicon and germanium *J. Appl. Phys.* **36** 153–6
[67] Hopcroft M A, Nix W D and Kenny T W 2010 What is the Young's modulus of silicon *J. Microelectromech. Syst.* **19** 229–38
[68] Li X, Ono T, Wang Y and Esashi M 2003 Ultrathin single-crystalline-silicon cantilever resonators: fabrication technology and significant specimen size effect on Young's modulus *Appl. Phys. Lett.* **83** 3081–3
[69] Ando T, Sato K, Shikida M, Yoshioka T, Yoshikawa Y and Kawabata T 1997 Orientation-dependent fracture strain in single-crystal silicon beams under uniaxial tensile conditions *Proc. Int. Symp. on Mechatronics and Human Science (5–8 October)* pp 55–60
[70] DelRio F W, Cook R F and Boyce B L 2015 Fracture strength of micro- and nano-scale silicon components *Appl. Phys. Rev.* **2** 021303